Salt-Mediated Coarsening in Conversion-Reaction-Synthesized Nanoporous Metals and Nanocomposites Resolved through *In Situ* Synchrotron Diffraction Studies

Adam A. Corrao, Gerard S. Mattei, Christopher M. Coaty, Zhuo Li, Victoria Petrova, Liang Yin, Ping Liu, and Peter G. Khalifah*

Read Online

ACCESS | Metrics & More | Article Recommendations | Supporting Information

ABSTRACT: High-energy synchrotron X-rays were used to probe the structural and microstructural evolution in Fe, Co, and Cu nanoporous metals (NPMs) and metal/salt nanocomposites (NCs) produced by recently developed conversion reaction synthesis (CRS) methods. Microstructure analysis of as-synthesized samples via whole pattern fitting showed that the NPMs exhibit domain sizes that increase as Co < Fe < Cu, with both Fe and Co having crystallite sizes below 3.0 nm. The as-synthesized metal/salt NCs had similar metal sizes, and additionally, the salt in the composite had unusually large lattice microstrain whose origin is attributed to chemical substitution of metal ions into the salt (e.g., $Li_{1-3x}Fe_xCl$ for Fe^{3+}). When thermal annealing is used to modify crystallite size, pore collapse often occurs in NPMs but NCs can be effectively tuned without this problem. While the NC coarsening occurs slowly at low temperatures, it was found that there is a drastic acceleration of the reaction rate at a specific onset temperature that results in the crystallite size increasing by an order of magnitude in about a minute. Curiously, there was no evidence in the diffraction data for salt melting at this onset temperature. However, there was a sharp reduction in the salt chemical lattice strain at the onset temperature, indicating that rapid metal coarsening is facilitated by the salt. This behavior indicates an unexpectedly coupled reaction mechanism by which the metal ions needed for grain growth are supplied by the salt in a rate-limiting fashion.
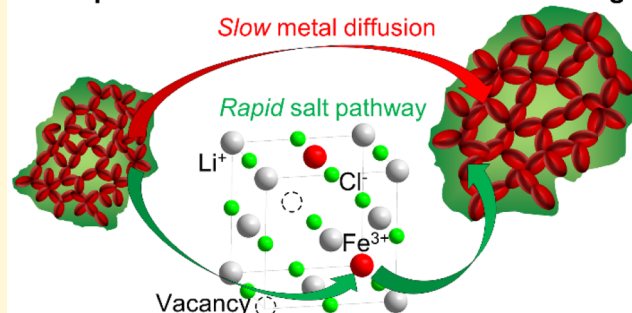
N anoporous metals (NPMs) are of great interest for applications that benefit from a high surface area such as catalysis and energy storage.[1−4] Nanoporous metal catalysts offer advantageous size effects such as high surface area and low packing density, while their pores can permit rapid mass transport.[4] Beyond transport, porosity contributes to the functionality of these nanomaterials. For example, nanoporous battery electrodes effectively compensate for volume changes through lithiation/delithiation in comparison to bulk materials whose structure degrades through cycling, leading to loss of capacity and performance.[5,6] Nanoporous copper has also been shown to be effective as a 3D current collector in lithium metal batteries.[7]

Though conventional nanoparticles provide high surface areas, their utility for elevated catalysis applications is adversely affected by their tendency to sinter and coarsen, thus necessitating the use of support materials that introduce further cost and complexity. Furthermore, unsupported nanoparticles have more severe health risks due to the ease with which they can be volatilized or otherwise be transported. In contrast, NPMs can be prepared with micrometer-scale secondary particle sizes and are thus considerably more stable,

improving their functionality and mitigating their toxicity. Despite the numerous advantages of NPMs over conventional nanoparticles, challenges in NPM synthesis, particularly with morphological and compositional control, have limited their use in applications.[1,8]

Dealloying (the selective removal of the less-noble metal from an alloy) is one of the most popular and well-studied means of producing NPMs.[3,4,9−13] However, this synthesis method is limited in scope (only works for a few metals), in scale-up, and in morphological control.[11,14,15] A class of alternative NPM preparation methods is templating (e.g., filling the voids in a block copolymer with precursors to yield a nanostructure), though these methods share most disadvantages of dealloying.[1,2,16−18] While conventional NPM synthesis

methods have been extensively explored, their disadvantages limit the development and deployment of NPMs and highlight the need for a simple and broadly applicable NPM synthesis alternative.

In our recent work, reactions previously utilized during the operation of conversion-type battery electrodes[19] were adapted to the synthesis of NPM structures, leading to a facile, versatile, and scalable route to producing NPMs.[20] This method, conversion reaction synthesis (CRS), follows a simple, room-temperature reaction, $MX_n + nLi \rightarrow M + nLiX \rightarrow M$, where MX_n, a bulk transition-metal halide precursor, is reduced by n-butyllithium, nLi, yielding a metal/lithium-halide nanocomposite, nLiX, formed from the transition-metal precursor's halide bonding with Li. The lithium-halide salt portion of the bicontinuous nanocomposite (NC) is subsequently removed by dissolution with an organic solvent that the metal is both insoluble in and stable against, leaving behind a continuous NPM network. A key advantage of the CRS method is its applicability to both noble (Au, Ag) and non-noble (Fe, Co) metals.

A schematic of CRS procedures for preparing NCs (2nd column) and NPMs (3rd column) is presented in Figure 1,
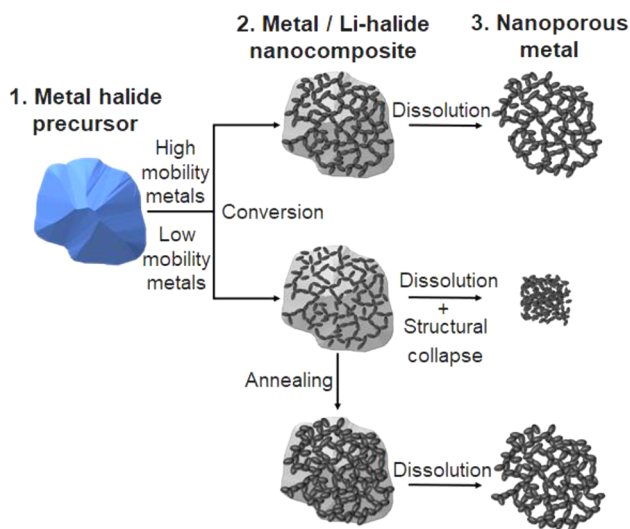

Figure 1. Three conversion reaction synthesis (CRS) routes to produce nanoporous metal (NPM) products, where nanocomposite annealing mitigates structural collapse during dissolution for low-mobility metals with small ligament sizes.

illustrating the synthesis steps as well as the expected results for postsynthesis annealing. In the case of NPMs with thin ligaments, dissolution of the salt support can result in collapse of the fragile metal framework, resulting in the loss of porosity and interior accessibility. In our previous work, we validated the use of thermal annealing for tuning the morphology of the intermediate metal/salt NCs prior to salt dissolution, showing that coarsening before salt removal can be used to prevent the structural collapse of NPMs during salt removal.[21] However, the lab XRD measurements and other *ex situ* characterization techniques (e.g., SEM, TEM, BET) used in that study provide limited insights into the coarsening mechanism.

We recently demonstrated that CRS-derived NPMs can exhibit improvements in catalytic activity relative to conventional nanoparticle metals.[22] However, access to a wide range of particle and pore sizes is needed, as different catalysis

applications have different optimal particle sizes and morphologies. For example, the smallest particle sizes have the highest accessible surface areas, but larger particle sizes have better resistance to coarsening during extended use at higher temperatures. Our long-term goal is to gain a quantitative understanding of the coarsening process, so that it is possible to dial-in a desired morphology by applying learned relationships between annealing conditions and particle and pore sizes instead of carrying out extensive empirical testing for each system of interest. Though coarsening processes in nanoparticle systems and NPMs produced by dealloying have been previously studied by *in situ* observations[23−25] and modeling,[26−28] the coarsening behavior and mechanisms appear to differ for CRS-derived NPMs and NCs, and thus are the focus of this work.

■ EXPERIMENTAL SECTION

Metal/salt nanocomposites (NCs) and nanoporous metals (NPMs) of Fe, Co, and Cu were synthesized via the CRS method.[20,21] Due to air and/or moisture sensitivity, precursor storage and synthesis was done in an argon glovebox (≤10 ppm of O_2; <1 ppm of H_2O). Reaction precursors were $FeCl_3$ (97% Sigma-Aldrich Product 157740), $CoCl_2$ (anhydrous beads 99.9% Sigma-Aldrich Product 449776), and $CuCl_2$ (anhydrous powder 99.995% Sigma-Aldrich Product 222011). In a typical synthesis, 2.0 g of metal chloride were dispersed in 20 mL of hexane (HPLC grade >95%, Sigma-Aldrich Product 439177) that was previous desiccated with molecular sieves (Type 3A, Sigma-Aldrich) for at least 48 h. Each chloride salt was dispersed in hexane and reacted with 1.6 M n-butyllithium in hexane (Sigma-Aldrich Product 186171) which was added in 25% excess to the amount needed for a stoichiometric reaction to help drive the reaction to completion. After 24 h, the solids were removed by filtration and rinsed 3× with 30 mL of hexane. The resulting metal/LiCl NC powder was dried in an argon glovebox. NPMs were obtained from the NCs by rinsing 3× with 30 mL of methanol to dissolve soluble chlorides and then drying.

For *ex situ* annealing experiments, aliquots of the as-synthesized NCs or NPMs were sealed in individual 19.5 mm OD borosilicate glass ampules (Kimble-Chase part # 12010U-10), placed in a preheated box furnace for 3 h, and then quenched to room temperature. The glass ampules were returned to the glovebox to extract the powders for further characterization. Powders for *ex situ* synchrotron studies were packed in 0.0435" OD Kapton tubing (Cole-Parmer item SK-95820-09) and sealed with epoxy. For *in situ* synchrotron annealing studies, powders were packed in borosilicate glass capillaries (0.9 mm ID, 1.1 mm OD) that were flame-sealed under vacuum.

Laboratory X-ray diffraction data were collected using a Bruker D2 Phaser powder diffractometer with a Cu Kα source ($\lambda = 1.5418$ Å, 40 kV, 40 mA) in a 2θ range of 10−80° at a scan rate of 0.01°/s. Data were collected using a divergence slit fixed at 0.6 mm, 250 mm beam path length, 20 mm sample length, and 2.5° Soller slits. Synchrotron X-ray diffraction data were collected in transmission mode on beamline 28-ID-2 (XPD) at the National Synchrotron Light Source-II (NSLS-II). The primary collection was done using an incident beam energy of 66.41 keV ($\lambda = 0.1867$ Å) with a 0.2 × 0.2 mm beam size, recording patterns on a 2D area detector (PerkinElmer XRD 1621, 2048 × 2048 pixel array, 200 × 200 μm pixel size) at a distance of 1418 mm providing data out to $d_{min} = 0.76$ Å. *Ex situ* data were collected with a default of 600 frames acquired during a 60 s total collection time, while *in situ* annealing data on Fe/LiCl was collected with 100 frames acquired during a 10 s total collection time. *In situ* annealing data on Co/LiCl and Cu/LiCl NCs was collected in a second experiment with a sample-to-detector distance of 1352 mm and an incident beam energy of 66.91 keV ($\lambda = 0.1853$ Å), using a total collection time of 10 s and 100 frames.

In situ annealing experiments were carried out in a flow cell furnace[29] using a Eurotherm 2408 temperature controller and a TDK
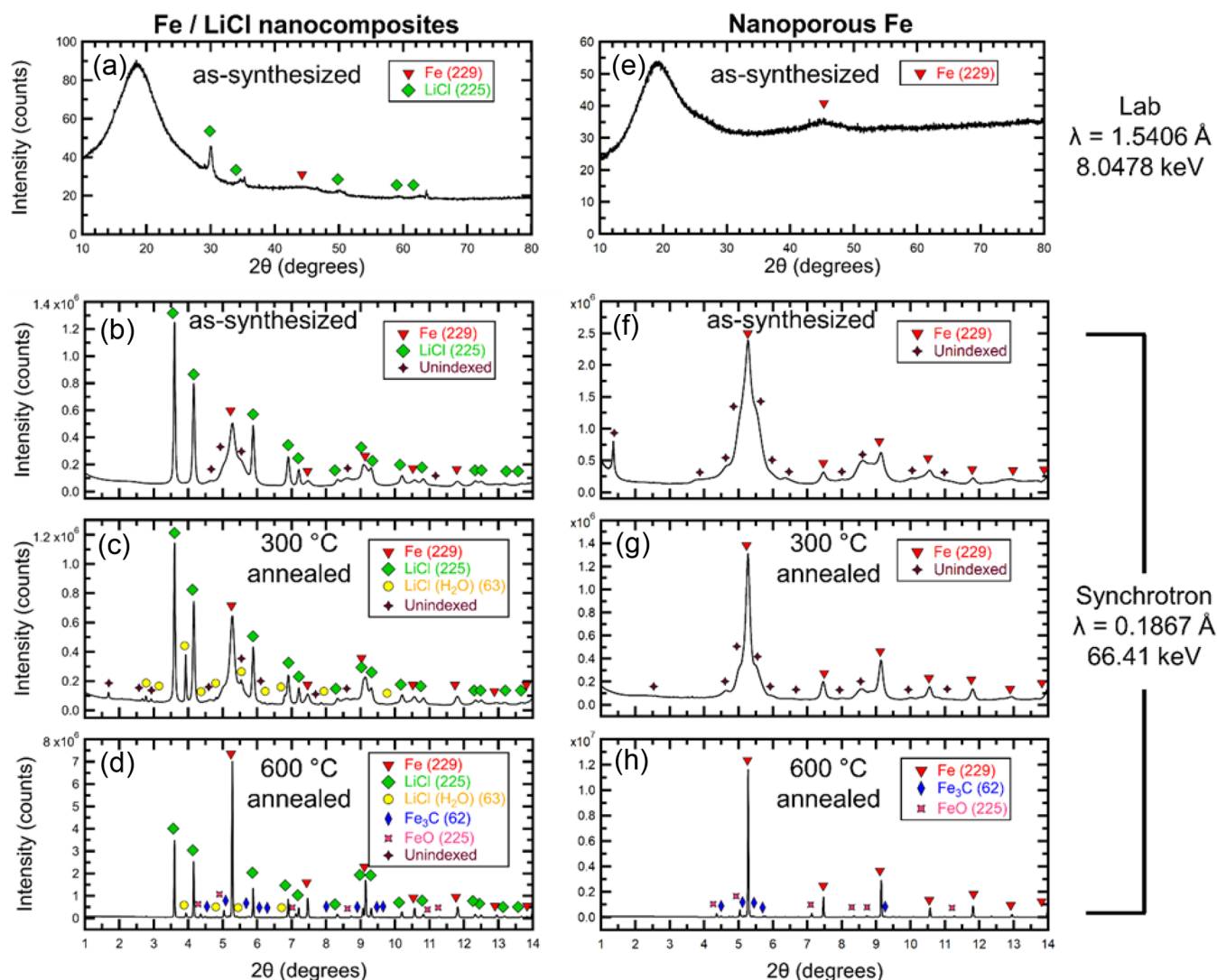
Figure 2. XRD patterns of Fe/LiCl nanocomposites (left) and Fe nanoporous metals (right). (a) Lab XRD pattern of an as-synthesized Fe/LiCl NC. (b−d) Synchrotron XRD patterns from Fe/LiCl NCs as-synthesized samples, annealed at 300 °C and annealed at 600 °C, respectively. (e) Lab XRD pattern of an as-synthesized Fe NPM. (f−h) Synchrotron XRD patterns from Fe NPMs samples as-synthesized, annealed at 300 °C, and annealed at 600 °C, respectively.

Lambda 900 W (30 V/30 A) power supply. Two heating elements were wound from resistive wire (Kanthal A-1, #24 awg) into coils, with temperature monitored using a K-type thermocouple (stainless steel, 0.01" OD, Omega Engineering item # KMQSS-010-6), with a picture of the furnace installed in the synchrotron shown in Figure S1. For the Fe/LiCl NC, the temperature was ramped to 525 °C over ∼2 h (4.7 °C/min) and then held 1 h, with data collected every 1 min. Similarly, the Co/LiCl NC program was an ∼1 h ramp (scan every 30s) to 500 °C (7.7 °C/min), with a 10 min hold at 500 °C (scan every 10 s), while that for Cu/LiCl NC was an ∼1 h ramp (scan every 30 s) to 500 °C (7.8 °C/min), with a 50 min hold at 500 °C (scan every 1 min).

Prior to autointegration, the instrument geometry (sample-to-detector distance, detector tilts, oblique incidence effect) was calibrated using data from a Si standard (Gem Dugout, $Fd\bar{3}m$, a = 5.43042) using GSAS-II.[30] The instrumental contribution to peak profiles was modeled using a modified Thompson−Cox−Hastings pseudo-Voigt (TCHZ) function optimized against the response from the Si standard and then fixed for sample refinements. Phase identification was done using JADE v.9 (MDI), against reference patterns in the International Centre for Diffraction Data (ICDD) database.[31] When automated search and match methods failed,

indexing methods were utilized in both the JADE and the TOPAS software package (Version 6, Bruker AXS).[32] For confirmation of the indexing, Pawley and Rietveld refinements were done in TOPAS. A custom python infrastructure was used to carry out sequential refinements on *in situ* diffraction data and automatically extract values of parameters of interest (e.g., crystallite size, microstrain, and phase fractions) for the thousands of patterns studied in this work. Representative TOPAS input files are provided as Supporting Information.

■ RESULTS AND DISCUSSION

Nanoporous metals (NPMs) prepared through conversion reaction synthesis (CRS) are in many ways ideally suited for catalysis applications. In order to fully realize their potential for catalysis, it is important to be able to gain precise control over their morphology, especially their primary particle size. The present work is therefore aimed at understanding the coarsening behavior during the thermal annealing of three representative nanoporous systems with different as-synthesized primary particle sizes, namely, Fe (∼3 nm), Co (∼2 nm), and Cu (∼25 nm).
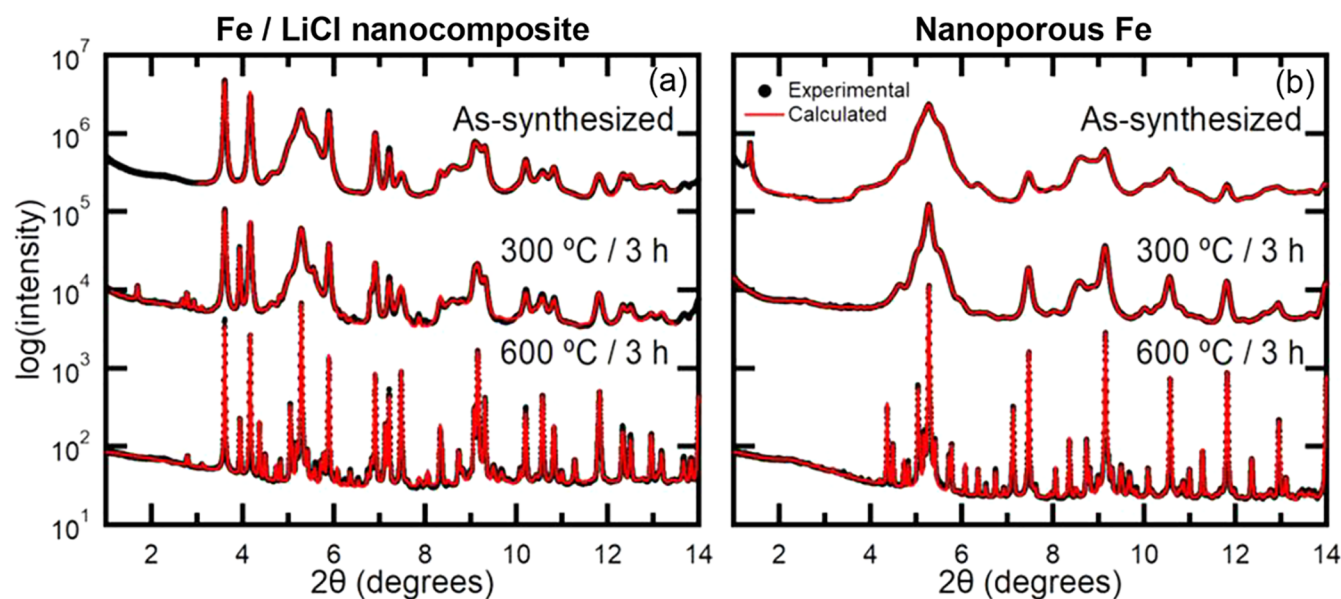
Figure 3. Fitting from Rietveld refinement of synchrotron XRD patterns for (a) Fe/LiCl NCs and (b) Fe NPMs. Results for as-synthesized (top), annealed at 300 °C (middle), and annealed at 600 °C (bottom) samples are shown. The middle and top patterns were vertically offset by 3.3×10^6 and 6.0×10^6, respectively.

One general method for characterizing the size of nanoscale particles is X-ray diffraction. There are well-established methods for quantifying the primary particle size based on X-ray diffraction peak profiles, since smaller particle sizes lead to greater peak broadening. Although the Scherrer equation is often used for this purpose with the width of a single peak as the analysis input, it is typically more robust to obtain size information through whole pattern fitting, as this allows size broadening (varies as $1/\cos \theta$) and strain broadening ($\tan \theta$) effects to be deconvoluted. The size obtained in this manner is a volume-weighted mean column length, and this quantity (calculated with a shape factor of K = 1) will be referred to as the primary particle size in our discussion of the data. Representative laboratory X-ray diffraction data is shown in Figure 2 for a Fe NPM sample (e), as well as for a Fe/LiCl nanocomposite sample (a) that is an intermediate in the NPM synthesis. In both cases, only a single Fe peak is visible (red triangle), and the boundary between this very broad peak and the background cannot clearly be resolved.

Given the limitations of lab X-ray data, an extensive set of synchrotron X-ray diffraction data was collected to precisely quantify the primary particle size of as-synthesized and postannealed samples. As can be seen in Figure 2, the synchrotron data has a vastly improved signal/noise ratio and covers a much wider d-spacing range, allowing 7 distinct Fe diffraction peaks to be measured. Although the initial paper describing the CRS synthesis of nanoporous metal samples suggested that they may be amorphous based on the dearth of peaks in lab XRD patterns,[20] the enhanced ability of synchrotron XRD to resolve weak and broad peaks allow the observed diffraction peaks for all of the NPM and NC samples studied here to be quantitatively modeled as coming from a crystalline phase with severe size broadening, as will be discussed in detail later. High quality *ex situ* diffraction patterns were collected in 60 s, which suggests the viability of *in situ* experiments to study morphological changes as they occur during heating.

***Ex Situ* Phase Identification.** In order to gain initial insights into the changes that occur during heating, high quality synchrotron diffraction patterns were collected *ex situ* for a series of three samples (as-synthesized, annealed at 300 °C for 3 h, annealed at 600 °C for 3 h) for each metal (Fe, Cu, Co), both for the NC reaction intermediate and for the NPM reaction product. Representative patterns for the Fe sample used for indexing are shown in Figure 2, while whole-pattern fits to confirm the indexing results are shown in Figure 3. The analogous data for the Co and Cu samples are provide in Figures S2–S5.

The extreme nanoscale nature of the as-synthesized Fe NPM sample can be seen clearly in Figure 2f. There are only a few obvious Fe diffraction peaks, and these peaks are very broad. Coarsening results in significantly sharper diffraction peaks after heating at 300 °C and extremely sharp diffraction peaks after treatment at 600 °C, consistent with preliminary lab X-ray testing done prior to this work.[21]

The sharpening of diffraction peaks makes it easier to resolve secondary phases in the Fe NPM patterns. In the 600 °C pattern, peaks matching those expected for $Fe_{1−x}O$ ($Fm\bar{3}m$, #225) and Fe_3C ($Pnma$, #62) can account for all non-Fe peaks. Both of these phases are plausible impurities. It has been previously observed that metal carbides can form from the reaction of *n*-butyllithium with metal chlorides, and similarly, incomplete removal of either H_2O or O_2 would be expected to be capable of oxidizing the surface of nanoscale Fe.[33] Secondary phases can also be seen in the 300 °C and as-synthesized patterns, though those peaks (Table S1) could not be matched to any plausible known phase and thus remain unindexed. One possibility is that they correspond to an alternate structure incorporating the same chemical impurities, especially since FeO is known to be thermodynamically unstable below 570 °C.[34] Based on the relative peak intensities, the observed impurities are expected to comprise at most a few percent of the sample mass, and it should be further noted that none of these peaks were observable in the lab X-ray diffraction data.

The Fe NC diffraction patterns have many similarities with the Fe NPM patterns, though with the addition of intense LiCl peaks and occasionally minor LiCl hydrate (LiCl·H_2O, *Cmcm*, #63) peaks that indicate the samples can react with moisture during their initial reaction or during the preparation of sealed capillaries for synchrotron studies. Impurity peaks corresponding to Fe_3C and FeO are again seen in the 600 °C pattern. Similar unindexed peaks are again seen, though these are now observed at all temperatures that were probed.

As a final check of the completeness of the pattern assignments, whole pattern fitting was carried out and is shown on a log scale in Figure 3. Known major phases (Fe, LiCl) and known secondary phases (Fe_3C, FeO, LiCl hydrate) were treated in a Rietveld manner while the unknown impurity peaks and the major glass peak were fit as independent peaks. The fits confirmed that all intensity in the patterns could be effectively captured in these models, which are therefore very suitable for quantitative microstructural analysis, as will be discussed in the next section.

The Co and Cu samples were analyzed in a similar manner to the Fe samples (Figures S2−S5). On the whole, the behavior was quite similar aside from the necessarily different nature of the metal-specific secondary phases such as unreacted $CoCl_2$ (attributed to large precursor particles that did not fully react) or the mixed salt Li_2CoCl_4.[35] Unlike the other metals, Co was observed to crystallize in two different polymorphs, one which is hexagonal close packed (hcp) and one which is cubic close packed (ccp). The ccp Co polymorph is well-known to be the thermodynamic equilibrium state in bulk samples prepared at high temperatures, though it is also well-known that the hcp Co polymorph can be easily formed during the preparation of nanoscale Co metal at low temperatures.[36−39] Both of these Co phases can exhibit stacking faults, and as a result of their complex peak shapes, there are larger differences between the observed and modeled patterns than for those of the other metals. Some Co and Cu NPM samples had peaks from small amounts of LiCl hydrate from incompletely washed LiCl. The Cu patterns were in general the simplest to model as they had both the sharpest diffraction peaks (due to their larger particle size) and the smallest contribution of impurity peaks.

Although a detailed model of the stacking faults in the Co samples is beyond the scope of this work, some further comments on the faulting can be made. In the hcp Co metal phase, the peak shapes problems are particularly pronounced for the 10*l* reflections, as highlighted for the 102 (2θ = 7.2°) and 104 (2θ = 11.6°) reflections in Figure S6. In both cases, the modeled peak shape is substantially sharper than the observed peak shape, an effect which persists even in the sample annealed at 600 °C. This specific behavior is more consistent with growth faults (e.g., ABABCBCB) than deformation faults (e.g., ABABCACA), as the former have been observed to be more resistant to repair through annealing.[38,40,41] In general, the 10*l* reflections with *l* = odd can be reasonably modeled with pseudo-Voigt peak shapes while those with *l* = even cannot, even after thermal annealing. Despite these complexities, it was found that the size and strain values obtained through fitting are largely unaffected by inclusion or exclusion of these exceptionally broadened peaks.

***Ex Situ* Microstructure Analysis.** The high quality of the present synchrotron diffraction data provides opportunities for the precise quantitative analysis of sample microstructure that are not accessible when using lab X-ray data. As illustrated in

the previous section, the fits to the peak profiles of the NC and NPM phases (e.g., Figure 3) are generally excellent with the minor exception of the Co metal phases for which the stacking faults cause small problems with the peak profiles. The samples should therefore be considered to have somewhat larger uncertainties in the refined Co crystallite sizes that are not captured in the statistical esds obtained from refinements. Furthermore, two different sizes will be reported for the hcp and ccp polymorphs of Co metal. The key quantities of interest obtained from these fits are the metal size (Figure 4a) and the LiCl salt strain (Figure 4b), with the values recorded in Tables S2−S4.
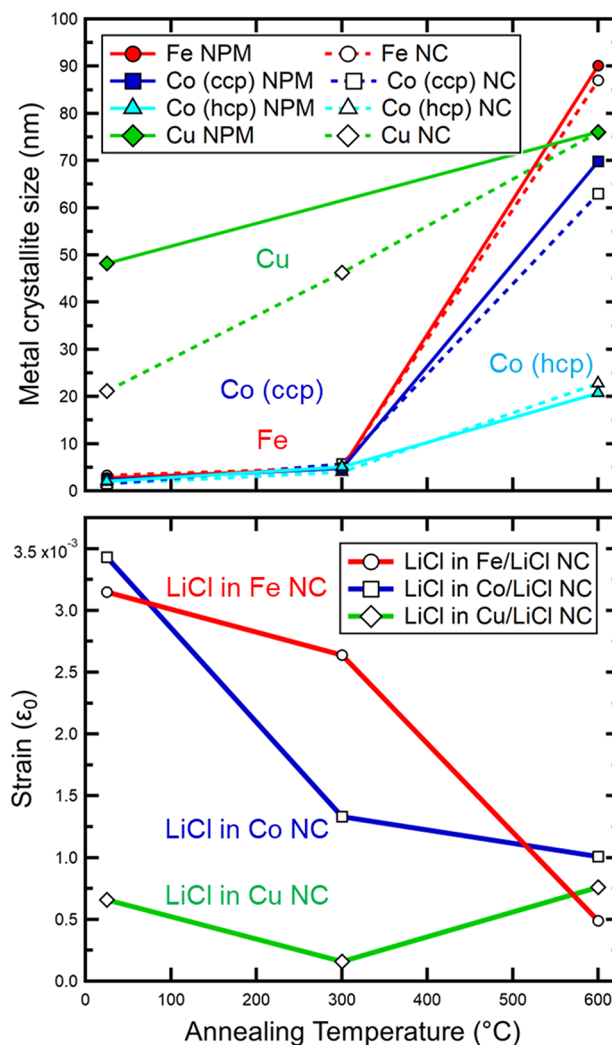

Figure 4. (a) Metal (Fe, Co, and Cu) crystallite size refined for nanoporous metals (solid lines) and metal/salt nanocomposites (dashed lines). (b) LiCl lattice chemical microstrain refined for metal/salt nanocomposites.

From the analysis of crystallite size obtained through Rietveld refinement, some conclusions can be made. For the NC reaction intermediates, the particle size increases in the order Co (1.5 nm hcp; 1.5 nm ccp) < Fe (3.2 nm) < Cu (21.2 nm), with the Cu sample being about an order of magnitude larger than the other phases. While the relative particle sizes within these NPMs is noted to correlate with the self-diffusion coefficients of these metals determined from radiotracer
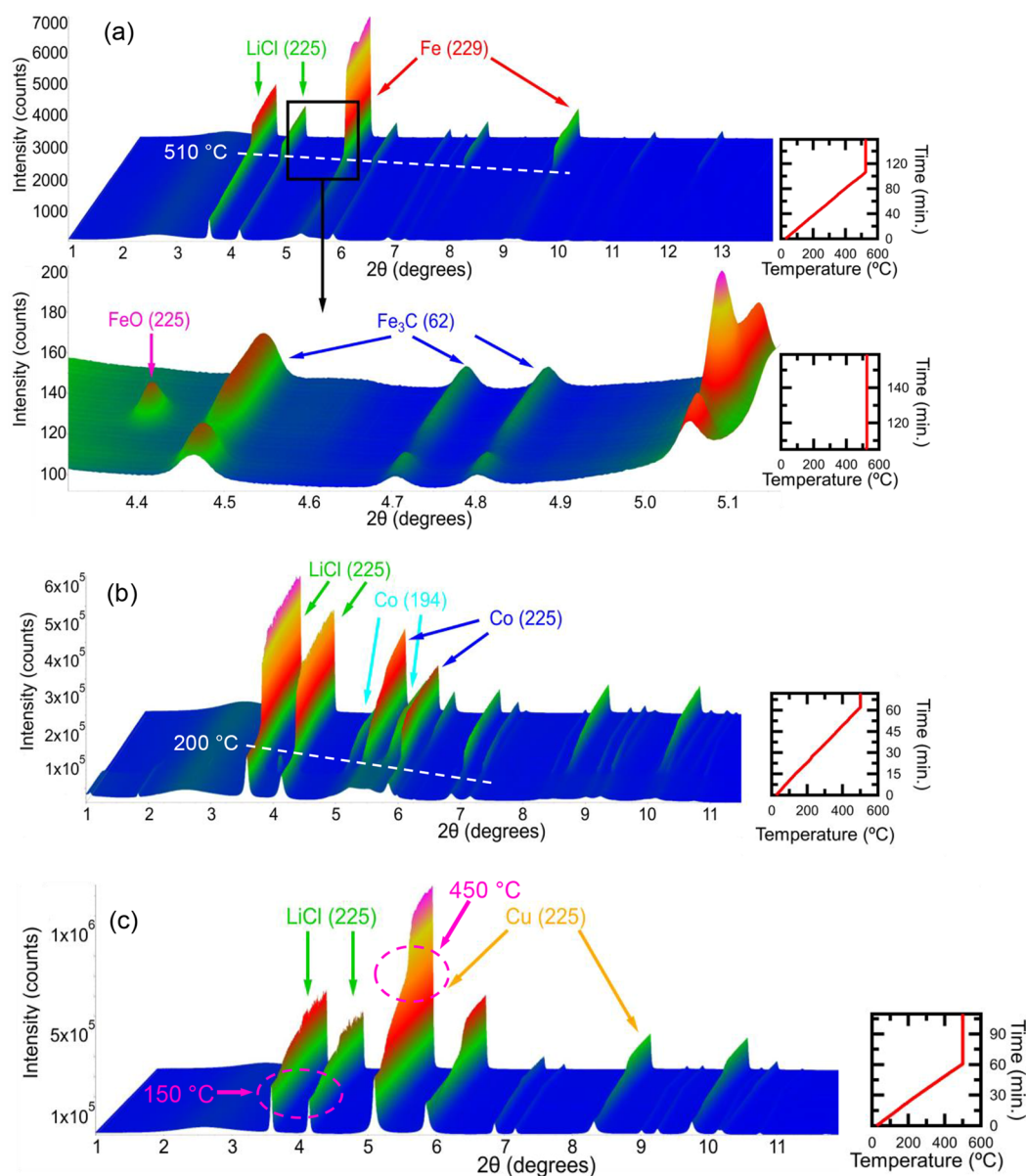
Figure 5. (a) Waterfall plot of XRD patterns from *in situ* annealing of Fe/LiCl NC with an ∼2 h heating ramp (1 min step between XRD patterns) from room temperature to 525 °C and a 1 h hold at 525 °C (1 min step). Lower plot is a small region (4.2°−5.2°) highlighting peaks from FeO and Fe₃C. (b) Waterfall plot of XRD patterns from *in situ* annealing of Co/LiCl NC with a 1 h ramp (30 s step) from room temperature to 500 °C and a 10 min hold at 500 °C (10 s step). (c) Waterfall plot of XRD patterns from *in situ* annealing of Cu/LiCl NC with a 1 h ramp (30 s step) from room temperature to 500 °C and a 50 min hold at 500 °C (10 s step).

experiments,[42−47] our recent work demonstrates that this is correlation rather than causation[48] and that the rate of coarsening is determined by the mobility of relevant species in the salt phase rather than in the metal phase for reasons that will be discussed in more detail later.

After washing the NCs to form NPMs, the order of sizes remains Co (2.0 nm hcp, 2.3 nm ccp) < Fe (2.9 nm) < Cu (48 nm) for the NPMs, with these changes plotted in Figure S7. The size increase that is seen for Co and Cu hints that the heat generated during washing may be sufficient to drive some initial coarsening, even before the samples are treated in a furnace. The one outlier is the Fe NPM sample, whose refined particle size of 2.9 nm is slightly smaller than the particle size seen for the nanocomposite before washing (3.2 nm). This may indicate that the surface Fe atoms more easily oxidize,

react, or dissolve into the solvent wash in a manner that leads to smaller Fe metal domain sizes.

Finally, the sizes of the two different Co phases (hcp, ccp) are found to be quite similar in the as-synthesized and the 300 °C annealed samples, suggesting that a similar mechanism is responsible for their formation. However, the size of the ccp phase grows about 3× larger than that of the hcp phase after annealing at 600 °C, suggesting that this temperature provides sufficient mobility to enable the transformation of the metastable hcp phase to the thermodynamically stable ccp phase. This conclusion is supported by the larger ccp fraction seen in the NPMs annealed at this temperature (70/30 distribution, in contrast to the 30/70 distribution at lower temperatures). It has previously been reported that the crossover between the hcp and ccp phase having the greatest

thermodynamic stability occurs at 417 °C,[37,38] though it seems likely that this transition temperature is size-dependent, as are many other properties of nanoscale materials.[49−53]

Although the initial plan was to track changes in the metal particle size, during experiments it was noticed that there were large changes in the width of the LiCl salt peaks during the postannealing of samples (Figure 4b). Specifically, the salt microstrain was found to be strongly anticorrelated with the metal particle size. The as-synthesized and 300 °C NC samples of Fe and Co both exhibited large LiCl strains which were relieved on heating to 600 °C—a treatment that greatly increased the metal particle size. Similarly, the NCs of Cu which had large Cu particle sizes at all temperatures also had low salt strains at all temperatures. While strain broadening of diffraction peaks is often associated with mechanical strain, there is no reason to expect large mechanical strains in a system synthesized from a liquid at room temperature in the absence of applied pressure. Rather, the observed LiCl strains are most consistent with a chemical origin of strain. This would be expected if unreduced metal cations were incorporated into the salt reaction, resulting in salts with variable compositions of $Li_{1−3x}Fe_xCl$ (Fe^{3+}), $Li_{1−2x}Co_xCl$ (Co^{2+}), and $Li_{1−2x}Cu_{2x}Cl$ (Cu^{2+}). Based on published FACT salt phase diagrams,[54] it is expected that LiCl can accommodate large degrees of substitution by the present metal cations—about 5% substitution by Fe^{3+}, about 20% substitution by Co^{2+}, and an unknown but likely very large amount of substitution by Cu^{2+} due to the very close similarity of its ionic radius with that of Li^+.[55] Different degrees of chemical substitution will lead to different cell lattice parameters, and the width of the lattice parameter distribution will produce the LiCl microstrain broadening observed in diffraction patterns that we term chemical strain.

***In Situ* Annealing of Metal/LiCl Nanocomposites.** In contrast to *ex situ* diffraction studies which only supply a few snapshots of reaction progress, *in situ* diffraction studies provide the opportunity to continuously follow the coarsening processes that occur as samples are heated. The temperature program for annealing experiments involved a slow ramp up to a maximum temperature of about 100 °C below the 605 °C melting point of LiCl followed by a hold of about 1 h at this temperature, with diffraction patterns collected at least once a minute during the experiments. The changes that occurred during experiments are summarized as waterfall plots of the ~200 diffraction patterns collected for each of the three metals (Fe, Co, Cu) in Figure 5.

The changes that occur during the heating of the Fe/LiCl nanocomposite (Figure 5a) will be discussed first, as this system is generally representative of the changes that occur. At temperatures below 510 °C, the metal coarsening occurs slowly during heating with the refined particle size (Figure 6a), doubling from 3 to 6 nm over the 2 h period, with the resulting peak breadth changes being too small to visually resolve in the waterfall plot. However, as the temperature increases by 15 °C over the next 3 min to the final hold temperature of 525 °C, there is a dramatic acceleration of the reaction rate by many orders of magnitude with the primary particle size growing to exceed 100 nm (which is the practical upper limit for resolving size in the present experimental configuration). Although this stunning enhancement of the reaction rate above T_{onset} = 510 °C might be at first guessed to result from melting of the salt, the diffraction data do not show the loss of intensity of the LiCl diffraction peaks that would signify melting. They do,
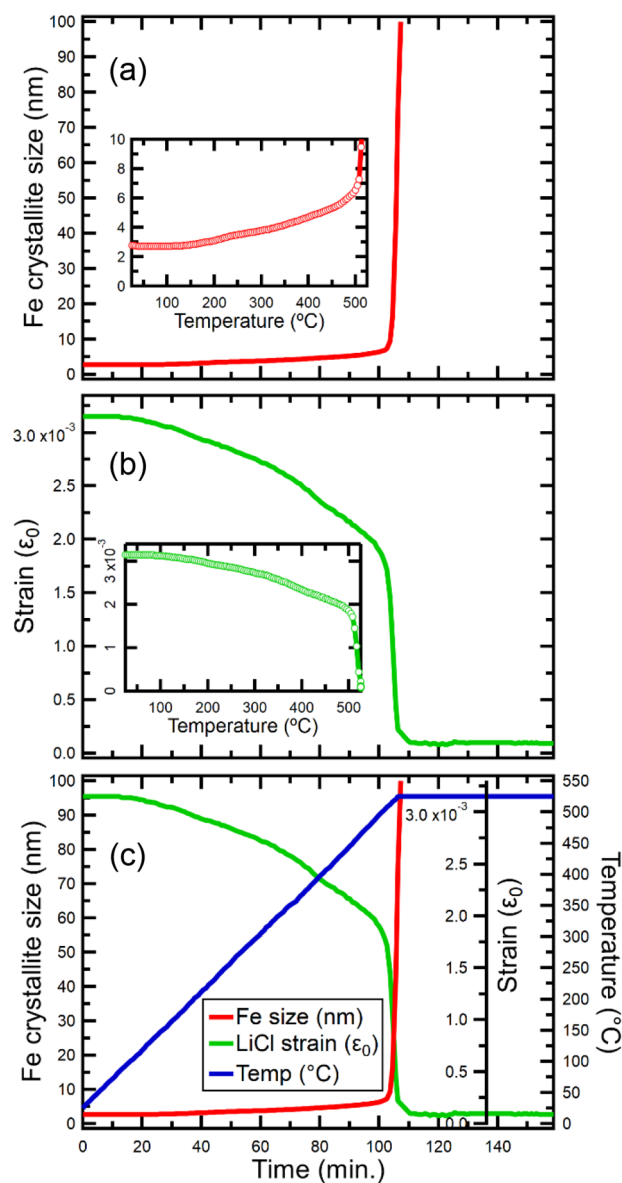

Figure 6. Results from size-strain analysis on XRD data from *in situ* annealing of an Fe/LiCl NC. (a) Fe crystallite size (nm) vs. time, with an inset highlighting the rapid acceleration in growth rate at 510 °C. (b) Strain in LiCl vs. time, with an inset showing a large drop at 510 °C. (c) Overlay of size, strain, and temperature vs. time highlighting the coupled mechanism of metal coarsening and salt strain reduction.

however, show another marked change at this temperature, with the peaks drastically sharpening. Quantitative fitting of the LiCl microstructure (Figure 6b) shows that this sharpening is due not to an increase in the LiCl particle size as would be expected in the case of full or even partial melting of this salt. In fact, the diffraction patterns at all times could be fit without including any size broadening contribution to the model. Instead, the sharpening of the LiCl peaks is due to a nearly complete reduction in the strain of the salt. The refined microstrain parameter ε_0 (as defined in the fundamental parameters approach of the TOPAS software as the maximum extent in the parabolic distribution of lattice strain, $\Delta d/d$)[56−58] gradually decreases from 3.2×10^{-3} to 1.8×10^{-3} during the temperature ramp from 25 to 500 °C and then abruptly drops from 1.5×10^{-3} to 0.1×10^{-3} between 510 and 525 °C,

indicating the nearly complete release of chemical strain from the salt.

This simultaneous onset of massive changes in the microstructure of both the Fe metal particles and the LiCl salt particles (Figure 6c) suggests that the rapid coarsening occurs through a correlated reaction mechanism in which the onset of rapid mass transport through the salt permits the very rapid coarsening of the metal. Similar behavior is seen for the other two metal nanocomposites studied in this work, though with even lower onset temperatures observed for Co ($T_{onset} \sim$ 200 °C) and Cu ($T_{onset} \sim$ 425 °C). These temperatures are far below any plausible eutectic points for the LiCl–CoCl$_2$ and LiCl–CuCl$_2$ systems, leading to the conclusion that there is an unexpected and likely novel salt-mediated solid state reaction pathway that enables rapid coarsening in these nanocomposite systems.

■ DISCUSSION

In general, the mass transport needed to grow the grains of a solid produced through a chemical reaction occurs through either bulk or surface processes. These distinct transport processes tend to have different activation energies, with the energies typically being lower for surface processes due to the smaller number of bonds that need to be broken for an atom to move. The overall reaction rate depends on not just the activation energy but also on the abundance of paths, and thus either surface or bulk transport processes can dominate the reaction mechanism. However, since the kinetics of both bulk and surface processes are governed by Boltzmann principles, the massive acceleration of the coarsening rate that occurs at T_{onset} is not consistent with the normal temperature-induced variation in reaction kinetics for a given process. Instead, it is characteristic of a specific thermodynamic event.

In the case of the present nanocomposites, the large strain in the salt suggests that there is substantial incorporation (chemical substitution) of metal cations into the LiCl matrix. It is therefore appropriate to ask if the abrupt changes in the solubility and/or mobility of metal cations in a LiCl host could be responsible for the massive changes in reactivity that occur at T_{onset}. A first place to look for insights is in thermodynamic phase diagrams. A preliminary analysis identifies two possible features in the phase diagrams that may be associated with the onset temperature of massively enhanced mobility.

In case of the Fe/LiCl NC system, the onset temperature of 510 °C is very close to the predicted melting point of a ternary phase, Li$_2$FeCl$_4$, that can exist in equilibrium with the substituted rocksalt phase Li$_{1-2x}$Fe$_x$Cl in the FeCl$_2$–LiCl phase diagram (Figure 7a).[54,59,60] As a result of this phase relationship, the maximum solubility of Fe in rocksalt ($x \sim$ 0.20) is at the Li$_2$FeCl$_4$ melting temperature, with the solubility sharply decreasing above this temperature. One possible origin of the rate enhancement could be that once the temperature of the maximum solubility of Fe cations in LiCl is reached, further heating pushes isolated atoms of Fe out of the salt. These highly underbonded species would be highly reactive, and thus could lead to the rapid growth of Fe metal crystallites. However, this hypothesis has some inconsistencies with the observed behavior. First, the growth of metal nanoparticles through the addition of metal cations is a redox process, and there is not an obvious driving force for the reduction of large amounts of metal cations. Second, on heating from 510 to 525 °C, the refined particle sizes increased from 6 nm to more than 100 nm. It is implausible that there is a sufficient mass of Fe
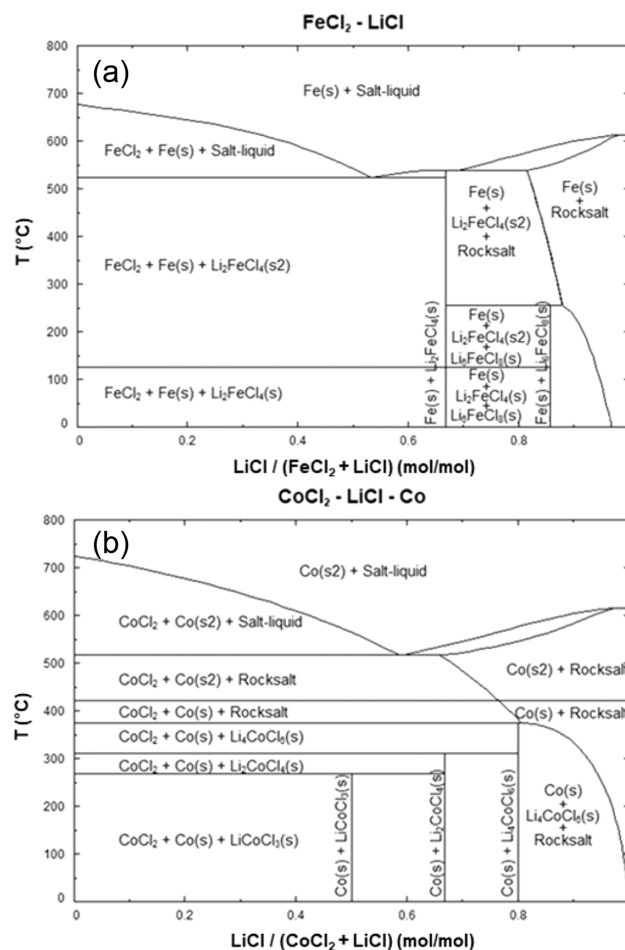

Figure 7. Phase diagrams for (a) FeCl$_2$–LiCl and (b) CoCl$_2$–LiCl, calculated in FactSage software from FactSalt databases.[54]

cations in the salt to account for the approximately 5,000-fold increase in particle volume (as calculated from the particle size change) through a purely additive process. Third, the much lower T_{onset} for the Co/LiCl system of 200 °C does not correspond to a similar drop in the solubility of Co cations in the LiCl lattice (Figure 7b).

An alternate hypothesis is that the massive reactivity enhancement that occurs at T_{onset} is due to the opening of a fast mass transport pathway. A plausible pathway is the conduction of metal species through the salt. This would presumably occur through three steps, (1) the oxidation of a neutral metal atom to a metal cation which enters the salt lattice, (2) the transport of the metal cation through the salt, and (3) the reduction of the metal cation to a neutral metal atom and its deposition/crystallization at a metal nanoparticle surface. This transport would be entirely analogous to solution-mediated ripening processes that occur via dissolution and recrystallization, though with the solid salt adopting the role of the high-mobility liquid solvent. Since the cumulative three-step process is charge-neutral, there is no net energy cost for the redox cycling of the metal atoms. Furthermore, if the redox cycling involves species of the same type [Co^0(site A) + Co^{2+}(site B) → (Co^{2+}(site A) + Co^0(site B)], it might be expected that the energy barriers for charge transfer are low.

In this scenario, there are a variety of possible mechanisms by which a fast metal transport pathway through the salt can open at a specific T_{onset}. One possibility would be an

enhancement of the salt mobility through either the creation of vacancies or the lowering of hopping barriers (e.g., through the elimination of strong repulsive interactions by the expulsion of metal cations from the LiCl host lattice). These changes could potentially be triggered by features in the thermodynamic phase diagrams, such as changes in cation solubility or the decomposition of phases such as Li_2FeCl_4 or $LiCoCl_3$ that may coexist and coherently intergrow with the salt. Another possibility for the origin of T_{onset} would be triggering enhanced access of the metal species to the salt, effectively opening a valve to access the high-mobility matrix. This could occur through turning on the reactions for redox cycling, either by barrier control or by depositing metal species that can undergo coupled redox reactions with the metal atoms at the surface of nanoparticles. Deposition processes could also be triggered by features in thermodynamic phase diagrams. An enhancement in surface area (e.g., introduction of porosity in the salt) or in mass transport across the interface (e.g., through partial melting at the surface) could also serve as a trigger for the massive enhancement in transport.

While the specific mechanism controlling the T_{onset} for rapid coarsening cannot be resolved from the present data, some robust insights have been gained from our pioneering in situ synchrotron studies. First, there is strong evidence that the salt is playing a noninnocent role in the reaction. In addition to the coupled metal and salt changes that occur at T_{onset}, it can also be seen at lower temperatures that the slower metal coarsening is occurring concomitantly with a gradual reduction in the salt strain. Second, the strain in the salt is chemical in nature and provides an important window into the transport processes that control coarsening. Third, there is no evidence that melting plays an important role in either the gradual or rapid coarsening processes. This can be concluded from the retention of the salt diffraction peaks during reactions, and perhaps more importantly, from the lack of a change in the particle size and crystallinity of the salt during these processes. These insights will guide the design of future experiments aimed at resolving the reaction mechanisms that govern the coarsening of metal/salt nanocomposites.

CONCLUSIONS

Nanoporous metals and metal/salt nanocomposites of Fe, Co, and Cu synthesized by conversion reaction synthesis have for the first time been studied using synchrotron X-ray powder diffraction. Ex situ studies enabled robust phase identification studies to be performed and provide precise microstructural information about both the metal and salt components. In situ studies revealed an unexpected dramatic acceleration of the coarsening reaction at a specific T_{onset} that is strongly metal-dependent. Furthermore, the increase in metal particle size was found to be accompanied by a decrease in the salt chemical strain, indicative of a coupled reaction mechanism and a noninnocent role of the salt in the metal coarsening. The observed coarsening behavior is very different from that previously seen for nanoporous metals produced through classic methods like dealloying.

Salts are often used as mineralizers in synthesis to greatly accelerate reactions and/or for sintering at temperatures above their melting point,[61−64] where the liquid salt can solubilize and transport cations. However, the present work is to the best of our knowledge the first instance in which a solid salt is responsible for a massive enhancement in reaction rates at temperatures far below the lowest melting eutectic of a system (more than 300 °C below the eutectic temperature of ~515 °C in the case of Co). Additionally, the reason for the sudden onset of fast transport (resulting in a thousand-fold increase in particle volumes in about a minute) remains to be resolved. Further in situ studies of coarsening reactions under a wider range of conditions are required to understand the complex interplay between the metal particle size, the salt chemical strain, and the reaction temperature that governs the reaction rate—studies that are ongoing. Intriguingly, the rapid reaction rates at low temperatures suggest that similar mass transport pathways may operate at room temperature during the conversion reaction synthesis and that understanding these pathways may lead to an improved understanding of and enhanced performance of important conversion type battery systems (e.g., FeF_3) that involve salts as key reaction intermediates.

■ ASSOCIATED CONTENT

Ⓢ Supporting Information

The Supporting Information is available free of charge at https://pubs.acs.org/doi/10.1021/acs.chemmater.2c03786.

> Beamline configuration, additional indexing and Rietveld refinement figures and discussion, peak profile and particle size evolution, unindexed peak tables, refinement parameter tables, extended discussion of the indexing of Co and Cu samples, protocols for and examples of fitting in situ diffraction data, and methods for phase diagram creation (PDF)
>
> Ex situ synchrotron diffraction data files (ZIP)
>
> TOPAS refinement control files for ex situ data (TXT)
>
> Exemplary TOPAS refinement control file for in situ data (TXT)

■ AUTHOR INFORMATION

Corresponding Author

Peter G. Khalifah − *Department of Chemistry, Stony Brook University, Stony Brook, New York 11794, United States; Chemistry Division, Brookhaven National Laboratory, Upton, New York 11973, United States;* ⓞ orcid.org/0000-0002-2216-0377; Email: kpete@bnl.gov

Authors

Adam A. Corrao − *Department of Chemistry, Stony Brook University, Stony Brook, New York 11794, United States; Chemistry Division, Brookhaven National Laboratory, Upton, New York 11973, United States;* ⓞ orcid.org/0000-0001-6111-8959

Gerard S. Mattei − *Department of Chemistry, Stony Brook University, Stony Brook, New York 11794, United States; Chemistry Division, Brookhaven National Laboratory, Upton, New York 11973, United States;* ⓞ orcid.org/0000-0003-3087-7762

Christopher M. Coaty − *Department of Nanoengineering, University of California—San Diego, La Jolla, California 92093, United States;* ⓞ orcid.org/0000-0002-8890-6389

Zhuo Li − *Department of Chemistry, Stony Brook University, Stony Brook, New York 11794, United States; Chemistry Division, Brookhaven National Laboratory, Upton, New York 11973, United States;* ⓞ orcid.org/0000-0001-6388-3398

Victoria Petrova − *Department of Nanoengineering, University of California—San Diego, La Jolla, California 92093, United States;* orcid.org/0000-0003-1917-4628

Liang Yin − *Department of Chemistry, Stony Brook University, Stony Brook, New York 11794, United States; Chemistry Division, Brookhaven National Laboratory, Upton, New York 11973, United States;* orcid.org/0000-0001-5396-782X

Ping Liu − *Department of Nanoengineering, University of California—San Diego, La Jolla, California 92093, United States;* orcid.org/0000-0002-1488-1668

Author Contributions

CMC prepared samples. AAC, GSM, ZL, LY, and CMC collected synchrotron X-ray diffraction data. AAC analyzed the diffraction data. AAC and PGK prepared the manuscript.

Notes

The authors declare no competing financial interest.

■ REFERENCES

(1) Zhang, J.; Li, C. M. Nanoporous Metals: Fabrication Strategies and Advanced Electrochemical Applications in Catalysis, Sensing and Energy Systems. *Chem. Soc. Rev.* **2012**, *41* (21), 7016−7031.

(2) Ding, Y.; Zhang, Z. *Nanoporous Metals for Advanced Energy Technologies*; Springer: 2016, DOI: 10.1007/978-3-319-29749-1_2.

(3) Guo, X.; Han, J.; Liu, P.; Chen, L.; Ito, Y.; Jian, Z.; Jin, T.; Hirata, A.; Li, F.; Fujita, T.; Asao, N.; Zhou, H.; Chen, M. Hierarchical Nanoporosity Enhanced Reversible Capacity of Bicontinuous Nanoporous Metal Based Li-O$_2$ Battery. *Sci. Rep.* **2016**, *6*, 33466 DOI: 10.1038/srep33466.

(4) Ding, Y.; Kim, Y. J.; Erlebacher, J. Nanoporous Gold Leaf: "Ancient Technology "/Advanced Material. *Adv. Mater.* **2004**, *16* (21), 1897−1900.

(5) Cook, J. B.; Lin, T. C.; Detsi, E.; Weker, J. N.; Tolbert, S. H. Using X-Ray Microscopy to Understand How Nanoporous Materials Can Be Used to Reduce the Large Volume Change in Alloy Anodes. *Nano Lett.* **2017**, *17* (2), 870−877.

(6) Yoshio, M.; Brodd, R. J.; Kozawa, A. *Lithium-Ion Batteries: Science and Technologies*; Springer: New York, 2009; DOI: 10.1007/978-0-387-34445-4.

(7) Lu, B.; Olivera, E.; Scharf, J.; Chouchane, M.; Fang, C.; Ceja, M.; Pangilinan, L. E.; Zheng, S.; Dawson, A.; Cheng, D.; Bao, W.; Arcelus, O.; Franco, A. A.; Li, X.; Tolbert, S. H.; Meng, Y. S. Quantitatively Designing Porous Copper Current Collectors for Lithium Metal Anodes. *ACS Appl. Energy Mater.* **2021**, *4* (7), 6454−6465.

(8) Sun, Y.; Liu, N.; Cui, Y. Promises and Challenges of Nanomaterials for Lithium-Based Rechargeable Batteries. *Nat. Energy* **2016**, *1*, 16071.

(9) Zhang, Z.; Wang, Y.; Qi, Z.; Zhang, W.; Qin, J.; Frenzel, J. Generalized Fabrication of Nanoporous Metals (Au, Pd, Pt, Ag, and Cu) through Chemical Dealloying. *J. Phys. Chem. C* **2009**, *113* (29), 12629−12636.

(10) Ding, Y.; Erlebacher, J. Nanoporous Metals with Controlled Multimodal Pore Size Distribution. *J. Am. Chem. Soc.* **2003**, *125*, 7772.

(11) Erlebacher, J.; Aziz, M. J.; Karma, A.; Dimitrov, N.; Sieradzki, K. Evolution of Nanoporosity in Dealloying. *Nature* **2001**, *410* (6827), 450−453.

(12) Erlebacher, J. An Atomistic Description of Dealloying. *J. Electrochem. Soc.* **2004**, *151* (10), C614.

(13) Van Petegem, S.; Brandstetter, S.; Maass, R.; Hodge, A. M.; El-Dasher, B. S.; Biener, J.; Schmitt, B.; Borca, C.; Van Swygenhoven, H. On the Microstructure of Nanoporous Gold: An X-Ray Diffraction Study. *Nano Lett.* **2009**, *9* (3), 1158−1163.

(14) Forty, A. J. Corrosion Micromorphology of Noble Metal Alloys and Depletion Gilding. *Nature* **1979**, *282*, 597−598.

(15) Pickering, H. W. Characteristic Features of Alloy Polarization Curves. *Corros. Sci.* **1983**, *23* (10), 1107−1120.

(16) Fahlman, B. D. *Materials Chemistry*; Springer: Dordrecht, 2007; DOI: 10.1007/978-1-4020-6120-2.

(17) Attard, G. S.; Bartlett, P. N.; Coleman, N. R. B.; Elliott, J. M.; Owen, J. R.; Wang, J. H. Mesoporous Platinum Films from Lyotropic Liquid Crystalline Phases. *Science (80-.)*. **1997**, *278* (5339), 838−840.

(18) Yamauchi, Y.; Suzuki, N.; Radhakrishnan, L.; Wang, L. Breakthrough and Future: Nanoscale Controls of Compositions, Morphologies, and Mesochannel Orientations toward Advanced Mesoporous Materials. *Chem. Rec.* **2009**, *9* (6), 321−339.

(19) Yu, S.-H.; Feng, X.; Zhang, N.; Seok, J.; Abruña, H. D. Understanding Conversion-Type Electrodes for Lithium Rechargeable Batteries. *Acc. Chem. Res.* **2018**, *51* (2), 273−281.

(20) Coaty, C.; Zhou, H.; Liu, H.; Liu, P. A Scalable Synthesis Pathway to Nanoporous Metal Structures. *ACS Nano* **2018**, *12* (1), 432−440.

(21) Coaty, C. M.; Corrao, A. A.; Petrova, V.; Khalifah, P. G.; Liu, P. Morphological Tuning of Nanoporous Metals Prepared with Conversion Reaction Synthesis via Thermal Annealing. *J. Phys. Chem. C* **2019**, *123* (29), 17873−17883.

(22) Coaty, C. M.; Corrao, A. A.; Petrova, V.; Kim, T.; Fenning, D. P.; Khalifah, P. G.; Liu, P. Anisotropic Nanoporous Morphology of ZnO-Supported Co That Enhances Catalytic Activity. *Nanoscale* **2021**, *13* (17), 8242−8253.

(23) Ingham, B.; Lim, T. H.; Dotzler, C. J.; Henning, A.; Toney, M. F.; Tilley, R. D. How Nanoparticles Coalesce: An in Situ Study of Au Nanoparticle Aggregation and Grain Growth. *Chem. Mater.* **2011**, *23* (14), 3312−3317.

(24) Chen-Wiegart, Y. C. K.; Wang, S.; Chu, Y. S.; Liu, W.; McNulty, I.; Voorhees, P. W.; Dunand, D. C. Structural Evolution of Nanoporous Gold during Thermal Coarsening. *Acta Mater.* **2012**, *60* (12), 4972−4981.

(25) Dai, Z. R.; Sun, S.; Wang, Z. L. Phase Transformation, Coalescence, and Twinning of Monodisperse FePt Nanocrystals. *Nano Lett.* **2001**, *1* (8), 443−447.

(26) Kolluri, K.; Demkowicz, M. J. Coarsening by Network Restructuring in Model Nanoporous Gold. *Acta Mater.* **2011**, *59* (20), 7645−7653.

(27) Erlebacher, J. Mechanism of Coarsening and Bubble Formation in High-Genus Nanoporous Metals. *Phys. Rev. Lett.* **2011**, *106* (22), 225504.

(28) Son, G.; Son, Y.; Jeon, H.; Kim, J. Y.; Lee, S. A Three-Dimensional Monte Carlo Model for Coarsening Kinetics of the Bi-Continuous System via Surface Diffusion and Its Application to Nanoporous Gold. *Scr. Mater.* **2020**, *174*, 33−38.

(29) Chupas, P. J.; Chapman, K. W.; Kurtz, C.; Hanson, J. C.; Lee, P. L.; Grey, C. P. A Versatile Sample-Environment Cell for Non-

Ambient X-Ray Scattering Experiments. *J. Appl. Crystallogr.* **2008**, *41* (4), 822−824.

(30) Toby, B. H.; Von Dreele, R. B. GSAS-II: The Genesis of a Modern Open-Source All Purpose Crystallography Software Package. *J. Appl. Crystallogr.* **2013**, *46* (2), 544−549.

(31) Gates-Rector, S.; Blanton, T. The Powder Diffraction File: A Quality Materials Characterization Database. *Powder Diffr.* **2019**, *34* (4), 352−360.

(32) Coelho, A. A. TOPAS and TOPAS-Academic: An Optimization Program Integrating Computer Algebra and Crystallographic Objects Written in C++. *J. Appl. Crystallogr.* **2018**, *51* (1), 210−218.

(33) Chang, Y. H.; Chiu, C. W.; Chen, Y. C.; Wu, C. C.; Tsai, C. P.; Wang, J. L.; Chiu, H. T. Syntheses of Nano-Sized Cubic Phase Early Transition Metal Carbides from Metal Chlorides and n-Butyllithium. *J. Mater. Chem.* **2002**, *12* (8), 2189−2191.

(34) Young, D. J. *High Temperature Oxidation and Corrosion of Metals*, 2nd ed.; Elsevier: 2016. DOI: 10.1016/C2014-0-00259-6.

(35) Kanno, R.; Takeda, Y.; Takahashi, A.; Yamamoto, O.; Suyama, R.; Koizumi, M. New Double Chloride in the LiCl-CoCl$_2$ System: I. Preparation, Crystal Structure, Phase Transformation, and Ionic Conductivity of Li$_6$CoCl$_8$. *J. Solid State Chem.* **1987**, *71* (1), 189−195.

(36) Nishizawa, T.; Ishida, K. The Co (Cobalt) System. *Bull. Alloy Phase Diagrams* **1983**, *4* (4), 387−390.

(37) Lizárraga, R.; Pan, F.; Bergqvist, L.; Holmström, E.; Gercsi, Z.; Vitos, L. First Principles Theory of the Hcp-Fcc Phase Transition in Cobalt. *Sci. Rep.* **2017**, DOI: 10.1038/s41598-017-03877-5.

(38) Houska, C. R.; Averbach, B. L.; Cohen, M. The Cobalt Transformation. *Acta Metall.* **1960**, *8* (2), 81−87.

(39) Kitakami, O.; Sato, H.; Shimada, Y.; Sato, F.; Tanaka, M. Size Effect on the Crystal Phase of Cobalt Fine Particles. *Phys. Rev. B - Condens. Matter Mater. Phys.* **1997**, *56* (21), 13849−13854.

(40) Warren, B. E. *X-Ray Diffraction*; Dover Publications: 1990.

(41) Mitra, G. B.; Hadler, N. C. Stacking Fault Probabilities in Hexagonal Cobalt. *Acta Crystallogr.* **1964**, *17*, 817−822.

(42) Peterson, N. L. Self-Diffusion in Pure Metals. *J. Nucl. Mater.* **1978**, *69−70* (C), 3−37.

(43) Buffington, F. S.; Hirano, K.; Cohen, M. Self Diffusion in Iron. *Acta Metall.* **1961**, *9* (5), 434−439.

(44) Nix, F. C.; Jaumot, F. E. Self-Diffusion in Cobalt. *Phys. Rev.* **1951**, *82* (1), 72−74.

(45) Kuper, A.; Letaw, H.; Slifkin, L.; Sonder, E.; Tomizuka, C. T. Self-Diffusion in Copper. *Phys. Rev.* **1954**, *96* (5), 1224−1225.

(46) Maier, K. Self-diffusion in Copper at "Low" Temperatures. *Phys. status solidi* **1977**, *44* (2), 567−576.

(47) Bussmann, W.; Herzig, C.; Rempp, W.; Maier, K.; Mehrer, H. Isotope Effect and Self-Diffusion in Face-Centred Cubic Cobalt. *Phys. Status Solidi* **1979**, *56* (1), 87−97.

(48) Feng, S.; Petrova, V.; Corrao, A. A.; Wang, S.; Yang, K.; Khalifah, P. G.; Liu, P. Morphological Control of Nanoporous Copper Formed from Conversion Reaction Synthesis. *J. Phys. Chem. C* **2022**, *126* (35), 14878−14885.

(49) Guisbiers, G.; Kazan, M.; Van Overschelde, O.; Wautelet, M.; Pereira, S. Mechanical and Thermal Properties of Metallic and Semiconductive Nanostructures. *J. Phys. Chem. C* **2008**, *112* (11), 4097−4103.

(50) Sun, J.; Simon, S. L. The Melting Behavior of Aluminum Nanoparticles. *Thermochim. Acta* **2007**, *463* (1−2), 32−40.

(51) Safaei, A. Shape, Structural, and Energetic Effects on the Cohesive Energy and Melting Point of Nanocrystals. *J. Phys. Chem. C* **2010**, *114* (32), 13482−13496.

(52) Castro, T.; Reifenberger, R.; Choi, E.; Andres, R. P. Size-Dependent Melting Temperature of Individual Nanometer-Sized Metallic Clusters. *Phys. Rev. B* **1990**, *42* (13), 8548−8556.

(53) Couchman, P. R.; Jesser, W. A. Thermodynamic Theory of Size Dependence of Melting Temperature in Metals. *Nature* **1977**, *269* (5628), 481−483.

(54) Bale, C. W.; Bélisle, E.; Chartrand, P.; Decterov, S. A.; Eriksson, G.; Gheribi, A. E.; Hack, K.; Jung, I. H.; Kang, Y. B.; Melançon, J.; Pelton, A. D.; Petersen, S.; Robelin, C.; Sangster, J.; Spencer, P.; Van

Ende, M. A. FactSage Thermochemical Software and Databases, 2010−2016. *Calphad Comput. Coupling Phase Diagrams Thermochem.* **2016**, *54*, 35−53.

(55) Shannon, R. D. Revised Effective Ionic Radii and Systematic Studies of Interatomic Distances in Halides and Chalcogenides. *Acta Crystallogr., Sect. A* **1976**, *32* (5), 751−767.

(56) Halder, N. C.; Wagner, C. N. J. Separation of Particle Size and Lattice Strain in Integral Breadth Measurements. *Acta Crystallogr.* **1966**, *20* (2), 312−313.

(57) Balzar, D. X-Ray Diffraction Line Broadening: Modeling and Applications to High-Tc Superconductors. *J. Res. Natl. Inst. Stand. Technol.* **1993**, *98* (3), 321.

(58) Balzar, D.; Ledbetter, H. Voigt-Function Modeling in Fourier Analysis of Size- and Strain-Broadened X-Ray Diffraction Peaks. *J. Appl. Crystallogr.* **1993**, *26*, 97−103.

(59) Kanno, R.; Takeda, Y.; Takada, K.; Yamamoto, O. Phase Diagram and Ionic Conductivity of the Lithium Chloride-Iron(II) Chloride System. *Solid State Ionics* **1983**, *9−10*, 153−156.

(60) Kanno, R.; Takeda, Y.; Takahashi, A.; Yamamoto, O.; Suyama, R.; Kume, S. Structure, Ionic Conductivity, and Phase Transformation in New Polymorphs of the Double Chloride Spinel, Li$_2$FeCl$_4$. *J. Solid State Chem.* **1988**, *72* (2), 363−375.

(61) Dell'Agli, G.; Colantuono, A.; Mascolo, G. The Effect of Mineralizers on the Crystallization of Zirconia Gel under Hydrothermal Conditions. *Solid State Ionics* **1999**, *123* (1−4), 87−94.

(62) Ke, S.; Wang, Y.; Pan, Z. Synthesis of Nd$_2$Si$_2$O$_7$ Ceramic Pigment with LiCl as a Mineralizer and Its Color Property. *Dye. Pigment.* **2014**, *108*, 98−105.

(63) Del Nero, G.; Cappelletti, G.; Ardizzone, S.; Fermo, P.; Gilardoni, S. Yellow Pr-Zircon Pigments: The Role of Praseodymium and of the Mineralizer. *J. Eur. Ceram. Soc.* **2004**, *24* (14), 3603−3611.

(64) Reddy, M. V.; Subba Rao, G. V.; Chowdari, B. V. R. Preparation and Characterization of LiNi$_{0.5}$Co$_{0.5}$O$_2$ and Li-Ni$_{0.5}$Co$_{0.4}$Al$_{0.1}$O$_2$ by Molten Salt Synthesis for Li Ion Batteries. *J. Phys. Chem. C* **2007**, *111* (31), 11712−11720.

☐ Recommended by ACS